

# Thon rings from amorphous ice and implications of beam-induced Brownian motion in single particle electron cryo-microscopy

G. McMullan<sup>a,\*</sup>, K.R. Vinothkumar<sup>a</sup>, R. Henderson<sup>a</sup>

<sup>a</sup>*MRC Laboratory of Molecular Biology, Francis Crick Avenue, Cambridge, CB2 0QH, U.K.*

---

## Abstract

We have recorded dose-fractionated electron cryo-microscope images of thin films of pure flash-frozen amorphous ice and pre-irradiated amorphous carbon on a Falcon II direct electron detector using 300 keV electrons. We observe Thon rings [1] in both the power spectrum of the summed frames and the sum of power spectra from the individual frames. The Thon rings from amorphous carbon images are always more visible in the power spectrum of the summed frames whereas those of amorphous ice are more visible in the sum of power spectra from the individual frames. This difference indicates that while pre-irradiated carbon behaves like a solid during the exposure, amorphous ice behaves like a fluid with the individual water molecules undergoing beam-induced motion. Using the measured variation in the power spectra amplitude with number of electrons per image we deduce that water molecules are randomly displaced by mean squared distance of  $\sim 1.1 \text{ \AA}^2$  for every incident 300 keV  $e^-/\text{\AA}^2$ . The induced motion leads to an optimal exposure with 300 keV electrons of  $4.0 e^-/\text{\AA}^2$  per image with which to see Thon rings centred around the strong  $3.7 \text{ \AA}$  scattering peak from amorphous ice. The beam-induced movement of the water molecules generates pseudo-Brownian motion of embedded macromolecules. The resulting blurring of single particle images contributes an additional term, on top of that from radiation damage, to the minimum achievable B-factor for macromolecular structure determination.

**Keywords:** Amorphous ice — Radiation damage — Thon rings — Markov Process — Noise whitening

---



---

\*Corresponding author

Email address: gm2@mrc-lmb.cam.ac.uk (G. McMullan)

## 1. Introduction

During the 1980s, Dubochet and his colleagues [2, 3] developed a method for carrying out electron cryo-microscopy (cryoEM) of biological structures embedded in thin films of amorphous ice. Their early work involved careful comparison of the conditions needed to obtain thin films of amorphous rather than hexagonal or cubic crystalline ice [2]. The method they developed consisted of rapidly freezing a thin film of water, or buffer solution, containing the biological structure of interest by plunging it into liquid ethane at a temperature just above that of liquid nitrogen. Images of the resulting specimen recorded using a suitable microscope could then be analysed to determine the structure. The method has since grown immensely in its power and popularity as improvements in technology have transformed its capability [4].

There has long been a debate within the electron cryo-microscopy community as to whether Thon rings [1] can or should be observed in power spectra of images of pure plunge-frozen amorphous ice. Thon rings arise naturally in bright-field phase contrast images of any amorphous material and their origin is described in most standard texts [5, 6]. The spacing and shape of the rings depend on the electron-optical parameters that describe the image, principally the amount of defocus and astigmatism. Thon rings from amorphous carbon are routinely used to adjust astigmatism and set the defocus of a microscope. Amorphous ice has approximately one half the density of amorphous carbon but as oxygen atoms scatter more strongly than carbon atoms [5] one might naively expect to see Thon rings of similar strength from amorphous ice and amorphous carbon.

In this paper we show that with the recently introduced CMOS direct electron detectors it is possible to see unambiguously Thon rings in images of high purity amorphous ice. The higher detective quantum efficiency, DQE, of the new detectors allows weaker signals to be seen and the ability to collect images continuously in a dose fractionated (or movie) mode allows optimal exposure conditions to be chosen and new modes of image processing to be used, long after the sample has been removed from the microscope.

## 2. Theory

### 2.1. Definitions

In this work the pixel value in an image at pixel  $(r, s)$  is denoted  $f_{r,s}$ , and scaled to units of  $e^-/\text{pixel}$ . The discrete Fourier transform,  $f(\mathbf{u})$ , at spatial frequency  $\mathbf{u}$  is calculated using

$$f(\mathbf{u}) = \sum_{r,s} f_{r,s} \exp(-i2\pi\mathbf{u} \cdot \mathbf{x}_{rs}). \quad (1)$$

and the power spectra,  $S(\mathbf{u})$ , calculated using the convention

$$S(\mathbf{u}) = \frac{1}{N_{\text{tot}}} |f(\mathbf{u})|^2 = \frac{1}{N_{\text{tot}}} \left| \sum_{r,s} f_{r,s} \exp(-i2\pi\mathbf{x}_{rs} \cdot \mathbf{u}) \right|^2. \quad (2)$$

### 2.2. Noise whitened power spectra

The modulation transfer function, MTF, and detective quantum efficiency, DQE, of the Falcon II detector are given in [7]. The MTF of the Falcon II drops rapidly with increasing spatial frequency corresponding to the Falcon II having a broad point spread function, PSF. For the combination of pixel size and sensitive layer thickness used in the Falcon II the PSF is chiefly determined by charge carrier diffusion in the sensitive layer rather than the scattering of incident electrons [7]. As a result the DQE of the Falcon II does not fall with the MTF. The strong spatial frequency dependence of the MTF is however reflected in the power spectra from the Falcon II and can make it difficult to see weak signals. In this case it is advantageous to use the noise whitened power spectrum,  $W(\mathbf{u})$ , given by

$$W(\mathbf{u}) = S(\mathbf{u})/\mathcal{N}(\mathbf{u}) \quad (3)$$

in which  $\mathcal{N}(\mathbf{u})$  is the normalised noise power spectrum [7]. For uniformly illuminated images, noise whitening removes the spatial frequency dependence of  $S(\mathbf{u})$  by boosting the signal at higher spatial frequencies. In particular it gives a flat background on which small signals can more easily be seen.

In [7] it was shown that for the Falcon II,  $\mathcal{N}(\mathbf{u})$  could be estimated directly from the measured modulation transfer function, MTF. Using  $\mathcal{N}(\mathbf{u})$  estimated in this way results in only a few percent variation in  $W(\mathbf{u})$  over the range from near zero to the Nyquist frequency in images with no sample present. In the present work it was found that the residual variation in  $W(\mathbf{u})$  with  $\mathbf{u}$  could be further reduced by using a fit to the measured  $S(\mathbf{u})$

with model for  $\mathcal{N}(\mathbf{u})$  consisting of only a radially symmetric function and its low order aliased terms. Note that while  $\mathcal{N}(\mathbf{u})$  is a two dimensional function almost all of the non-circularly symmetric components arise simply from the contributions of aliased terms. Details of the fitting procedure are given in the supplementary data.

### 2.3. Probability distribution for values in the noise whitened power spectra

For uniformly illuminated images the probability distribution for values of  $W(\mathbf{u})$  can be described using a single parameter. With no sample, the real and imaginary components of  $f(\mathbf{u})$  in Eq. (1) are independent Gaussian random variables [8]. As a result the squares of the real and imaginary components have  $\chi^2$  distributions and their sum,  $S(\mathbf{u})$ , an exponential distribution. Noise whitening sets the same average value, and hence exponential distribution for values of  $W(\mathbf{u})$ , at all spatial frequencies,  $\mathbf{u}$ . For any given spatial frequency,  $\mathbf{u}$ , the probability that  $W(\mathbf{u})$  has value  $y$  is therefore

$$\text{Prob}[y = W(\mathbf{u})] = \exp(-y/\Gamma)/\Gamma \quad (4)$$

in which  $\Gamma$  is the mean value of  $W(\mathbf{u})$ .

The DQE of the Falcon II detector is principally limited by the intrinsic variability of its response to individual electrons. If the average gain and variance in the gain are  $\bar{g}$  and  $\sigma_g^2$ , respectively, then the value of noise power spectrum in the limit of zero spatial frequency with  $n$  incident independent electrons per pixel is [9]

$$S(0) = \bar{g}^2 n + \sigma_g^2 n \quad (5)$$

and

$$\text{DQE}(0) = \bar{g}^2 / (\bar{g}^2 + \sigma_g^2). \quad (6)$$

Using Eqns. (3) to (6) gives

$$W(0) = W(\mathbf{u}) = n/\text{DQE}(0) = \Gamma \quad (7)$$

since the average value of  $W(\mathbf{u})$  is the same for all  $\mathbf{u}$ , by definition  $\mathcal{N}(0) = 1$  and expressing the detector output in units of incident electrons sets the gain to unity. The probability distribution for values of  $W(\mathbf{u})$  depends solely on  $\Gamma = n/\text{DQE}(0)$  via Eq. (4) and has both mean and standard deviation of  $\Gamma$ . In particular, for the Falcon II  $\text{DQE}(0) \sim 0.5$  [7] and so  $\Gamma \sim 2n$ .

### 2.4. Power spectra of Dose fractionated series

If a dose fractionated exposure consists of  $M$  frames with an average of  $d$  uncorrelated electrons per frame, from Eq. (7) the expected value of  $W_{M,m}$  defined as the sum of the  $M/m$  noise whitened power spectra from the images obtained by summing  $m$  consecutive frames is

$$W_{M,m} = \sum_i^{M/m} (md/\text{DQE}) = \frac{D_{\text{tot}}}{\text{DQE}}. \quad (8)$$

in which  $D_{\text{tot}} = Md$  is the total number of electrons in the exposure. Similarly the expected noise,  $N_{M,m}$ , in  $W_{M,m}$  is

$$N_{M,m} = \sqrt{\sum_i^{M/m} (md/\text{DQE})^2} = \frac{D_{\text{tot}}}{\text{DQE}} \sqrt{\frac{m}{M}}. \quad (9)$$

While the value of  $W_{M,m}$  is independent of  $m$ , the noise in sum,  $N_{M,m}$ , grows as the square root of  $m$ . In practice residual correlation in pixel values between frames, such as from an offset drift, will result in an  $m$  dependence in  $W_{M,n}$ . The actual Falcon II detector used here had a small correlated shift in the row-reset between successive frames that results in a 1% drop in  $W_{M,m}(\mathbf{u})$  between  $m = 1$  and  $m = 2$ . However the largest systematic correlation comes from the applied per pixel gain correction of the images which results in an increase in  $W_{M,m}(\mathbf{u})$  with increasing  $m$  but with careful gain calibration keeps the effect is less than 5% in going from  $m = 1$  and  $m = 120$ .

### 2.5. Effect of random motion of water molecules on power spectra

At any given instant there is typically only a single high energy electron interacting with the sample during a typical cryoEM exposure. An incident electron passing through a thin layer of amorphous ice will see a particular conformation of atoms but the radiation damage resulting from the interaction of the high energy electron with the amorphous ice will perturb the conformation of atoms in the ice [10]. Subsequent high energy electrons incident on the ice will see, and perturb, the atomic configurations resulting in a Markov-like process for the evolution of the atomic configuration. In reality possible atomic configurations in amorphous ice are strongly constrained by the ice rules of Bernal and Fowler[11]. The simplest approximation for

the transition probability of atom positions in going from one conformation to the next is to use a Gaussian distribution depending solely on the number of high energy electrons incident per unit area between the configurations. In particular if after  $n$  electrons per unit area the position of the  $i$ -th water molecule is  $\mathbf{x}_i(n)$ , after a further  $d$  electrons per unit area the probability distribution for its position has a Gaussian distribution

$$P(\mathbf{x}_i(n+d) : \mathbf{x}_i(n)) = \frac{1}{(2\pi d\sigma_0^2)^{3/2}} \exp \left\{ -\frac{|\mathbf{x}_i(n+d) - \mathbf{x}_i(n)|^2}{2d\sigma_0^2} \right\} \quad (10)$$

in which  $\sigma_0^2$  is the mean squared displacement in a given direction in response to a single incident electron per unit area.

Assuming an image consists of  $M$  frames and has a total exposure of  $D$  electrons per unit area. The power spectrum,  $S(\mathbf{u})$ , at spatial frequency  $\mathbf{u}$  in terms of the Fourier components,  $f_i(\mathbf{u})$ , of the  $i$ -th frame is

$$S(\mathbf{u}) \propto \langle |\sum_{i=1}^M f_i(\mathbf{u})|^2 \rangle = \sum_{i,j=1}^M \langle f_i^*(\mathbf{u}) f_j(\mathbf{u}) \rangle \quad (11)$$

where  $\langle \dots \rangle$  denotes an ensemble average. Since the average number of incident electrons per unit area in each frame is  $d = D/M$ , using Eq. (10) the  $|i-j|d$  incident electrons between  $i$ -th and  $j$ -th frames will randomly displace the water molecules so that

$$\langle f_i^*(\mathbf{u}) f_j(\mathbf{u}) \rangle \propto d^2 F_0(\mathbf{u})^2 \exp(-\alpha_u |i-j|d) \quad (12)$$

in which  $\alpha_u = 2\pi^2 \sigma_0^2 u^2$  and  $\sigma_0^2$  is the induced mean squared motion of a water molecules per incident electron though a unit area while  $F_0(\mathbf{u})^2$  is defined as

$$F_0(\mathbf{u})^2 \equiv \frac{1}{Md^2} \sum_{i=1}^M \langle |f_i(\mathbf{u})|^2 \rangle. \quad (13)$$

Substituting Eq. (12) into Eq. (11) and summing over  $i$  and  $j$  gives

$$S(\mathbf{u}) = d^2 F_0(\mathbf{u})^2 \times \left( \frac{2e^{-\alpha_u d}}{(1 - e^{-\alpha_u d})^2} \{ (1 - e^{-\alpha_u d})M + e^{-\alpha_u M d} - 1 \} + M \right). \quad (14)$$

In cases where there is very little induced movement  $\alpha_u \rightarrow 0$  so that  $S(\mathbf{u}) \rightarrow M^2 d^2 F_0(\mathbf{u})^2$  and since

$d = D/M$  we have  $S(\mathbf{u}) \propto D^2$ . On the other hand if there is no correlation between frames then  $\alpha_u \rightarrow \infty$  and  $S(\mathbf{u}) \rightarrow M d^2 F_0(\mathbf{u})^2$ .

For an exposure with a total of  $D$  electrons but where the molecules are continuously moving we can let  $M \rightarrow \infty$  and the summation in Eq. (11) goes over to an integral giving

$$S(\mathbf{u}) = 2F_0(\mathbf{u})^2 [\alpha_u D + \exp(-\alpha_u D) - 1] / \alpha_u^2 \quad (15)$$

which in the limits of small and large  $\alpha_u$  goes to  $D^2 F_0(\mathbf{u})^2$  and  $2DF_0(\mathbf{u})^2 / \alpha_u$ , respectively.

## 2.6. Estimation of beam induced movement from dose fractionated images

The amount of movement resulting from an incident electron can be estimated from the variation in Thon ring signal as a function of the number of incident electrons in an image. When the induced motion is smaller than a given spatial frequency the Thon ring modulation at that spatial frequency is expected to grow quadratically with the number of incident electrons in an exposure but as the induced motion becomes comparable with the spatial frequency the amplitude should grow more slowly. From Eq. (15) the power spectrum,  $S(u)$ , at a spatial frequency  $u$ , is expected to vary with total number of electrons per unit area,  $D$ , as

$$S(u) \propto 2[\alpha_u D + \exp(-\alpha_u D) - 1] / \alpha_u^2. \quad (16)$$

in which  $\alpha_u = 2\pi^2 \sigma_0^2 u^2$ , and  $\sigma_0^2$  is the mean-squared movement in a given direction per incident electron passing through a unit area. The actual Thon ring modulation does not appear explicitly in this equation but the Thon ring modulation enables the signal from the ice to be identified over the background noise in the measured power spectra. The measured spatial frequency dependence of  $S(u)$  will also include that of the detector but for the Falcon II detector this can be removed by using the noise whitened power spectra,  $W(u)$  as defined in Eq. (3).

From a single dose fractionated exposure it is possible to estimate  $\sigma_0^2$  through the dose dependence present in Eq. (16). If an the exposure consists of  $M$  frames each with an average of  $d$  elections per unit area, the result of summing the original frames in blocks of  $m$  is to produce  $M/m$  frames with on average  $md$  electrons per unit area. Denoting the sum of the resulting  $M/m$  noise whitened

power spectra by  $W_{M,m}(u)$  and using Eq. (16) gives

$$W_{M,m}(u) \propto \frac{2D_{\text{tot}}}{\alpha_u} (\alpha_u md + \exp(-\alpha_u md) - 1) / \alpha_u md \quad (17)$$

in which  $D_{\text{tot}} = Md$ . The behaviour of Eq. (17) with  $m$  depends only on  $z = \alpha_u md$  and is described by the functional form

$$g(z) = (z + e^{-z} - 1)/z. \quad (18)$$

This is a monotonically increasing function that initially varies linearly with  $z$  but plateaus towards 1 for large  $z$ . By fitting the non-linear behaviour of  $W_{M,m}(u)$  as a function of  $m$  it is possible to estimate  $\alpha_u$ , and hence obtain  $\sigma_0^2$ .

### 3. Experimental

Quantifoil R1.2/1.3 Cu/Rh grids were used to make a thin film sample of double distilled water (18 MΩcm conductivity). The grids were glow-discharged in air for 30-40 seconds and 3 μl of water applied in an environmental plunge-freeze apparatus [12]. Grids were blotted for 4-6 seconds and rapidly frozen in liquid ethane. The grids were transferred to Krios cartridges and imaged using a Falcon II direct electron detector on a FEI Titan Krios operated at 300 keV. A nominal magnification of 75,000x corresponding a calibrated value of 134,600x was used which results in a 1.04 Å sampling with the 14 μm pixels of the Falcon II detector. Imaging was performed using nano-probe mode with parallel illumination using a 70 μm C2 aperture and no objective aperture. A beam slightly larger and centred on the Quantifoil hole was used. Astigmatism and beam tilt correction were performed at the imaging magnification. Images were recorded at 18 frames/sec for either 8 or 17 seconds with either 2.33 e<sup>-</sup>/frame, or 0.85 e<sup>-</sup>/frame, respectively. The electron exposure per frame was determined from the screen current and average signal from the Falcon detector, with these being calibrated against a picoammeter as described previously [7].

The amorphous carbon control specimen was made in an Edwards 301 vacuum coating unit by evaporating carbon from an arc onto mica. The thickness of the carbon film was estimated to be 150 Å from the optical density of the carbon deposited on adjacent piece of filter paper. The carbon film was floated off the mica using a water bath

and placed onto a Cu/Rh grid. The continuous carbon grid was examined using the Atlas component of the FEI EPU software. From the Atlas an area of the carbon film was selected in which the carbon film had no holes or wrinkles both in the grid square and surround grid squares. After pre-irradiation of the carbon, images were recorded for 1.5 seconds with the same magnification and number of incident electrons per frames as used for the ice sample. The stage was moved to adjacent areas in a raster (using 0.4 μm steps in X followed by 0.4 μm steps in Y). A total of 25 images from different but adjacent areas of carbon film were collected with the defocus for all images set as close as possible to a nominal 5000 Å by manually adjusting the focus at each position. Later evaluation using CTFFIND3 [13] showed that the defocus was actually 5990 Å, with 200 Å of astigmatism and ±90 Å defocus variation over the 25 images.

Images were recorded using the full 4k×4k output of the Falcon II detector with the individual frames of all the images being captured using an in-house data capture setup. In processing the exposures the individual frames were not aligned computationally.

### 4. Results

Fig. 1 shows two types of noise whitened power spectra,  $W(u)$ , [7] from a dose fractionated exposure of pure amorphous ice consisting of 141 frames with on average 2.33 e<sup>-</sup>/pixel per frame. The spectrum from the sum of all the 141 frames is shown in Fig. 1(a) and with such a relatively high dose (300 e<sup>-</sup>/Å<sup>2</sup>) it is possible to see faint Thon rings. Fig. 1(b) shows the sum of the 141 noise whitened power spectra of the individual frames. Exactly the same images were used but in the sum of the power spectra of the individual images the Thon rings that are barely visible in Fig. 1(a) are clearly visible and can be seen to extend out beyond 3.4 Å resolution. The  $\sqrt{141}$  reduction in the noise from averaging the 141 individual spectra enables the strength of the Thon rings in individual frames to be seen clearly. The strength of this signal indicates that the Thon rings arise from the intrinsic bulk water and not from impurities absorbed from the adjacent carbon film or contamination occurring during the blotting and transfer steps.

The behaviour of the circularly averaged power spectra and circularly averaged noise whitened power

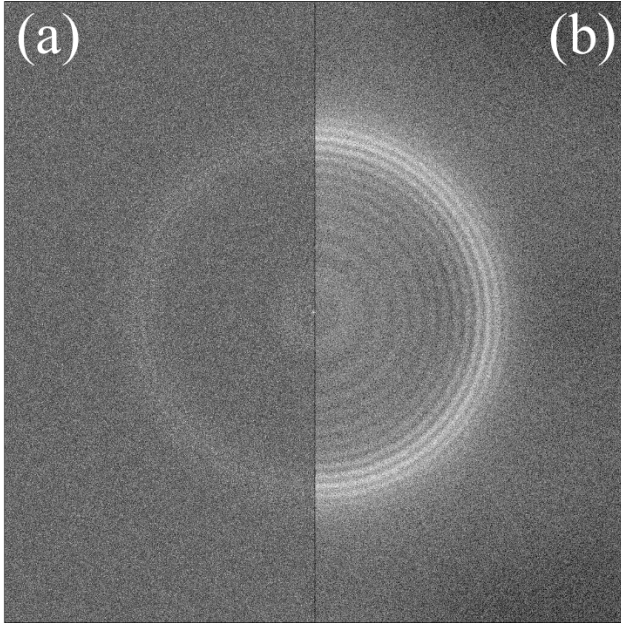


Figure 1: Thon rings from a dose fractionated exposure (image #230804) of amorphous ice obtained using either (a) the NWPS of the sum of the frames, or (b) the sum of the NWPS from each frame. The exposure consisted 141 frames at a dose of  $2.33 \text{ e}^-/\text{pixel}$  using 300 keV electrons, a defocus of  $7700 \text{ \AA}$  and a pixel sampling of  $1.04 \text{ \AA}$ . The edge of the transform is at  $1/2.08 \text{ \AA}^{-1}$  and the strong ring pattern in (b) is centred around  $1/3.7 \text{ \AA}^{-1}$ . In both (a) and (b) the images were first scaled so that the RMS noise level was 1 and then the lower and upper grey limits set at -0.7 and 1.3 about the mean values.

spectra are compared in Sec. SVI of the supplementary material. The flat, featureless backgrounds in Fig. 1(a) and Fig. 1(b) illustrate the success of the noise whitening procedure. The measured average value and noise in the noise whitened power spectra of Fig. 1 are within 5% of the values predicted by Eqs. (8) and (9) using  $n = 2.33$  and  $\text{DQE}(0) = 0.5$ . The probability distribution based on all the values in the 141 noise whitened power spectra used in Fig. 1(b) is given in Sec. SVII of the supplementary material. The distribution is well described by Eq. (4) with a measured value of  $\Gamma = 4.91$  that is within 5% of an estimated based on Eq. (7) again using  $n = 2.33$  and  $\text{DQE}(0) = 0.5$ .

To illustrate the origins of the difference between Fig. 1(a) and Fig. 1(b) we carried out two control experiments using amorphous carbon film. The amorphous carbon film was first pre-irradiated as even atoms in films of carbon prepared by evaporation from a carbon arc *in vacuo* move when initially irradiated. The amount of movement de-

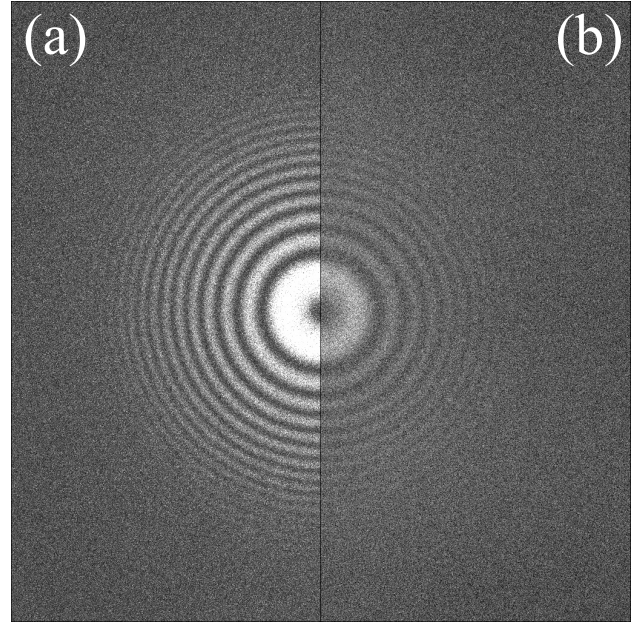


Figure 2: Comparison from a dose fractionated exposure of an area of pre-irradiated carbon of (a) the NWPS obtained from the sum of all the frames and (b) the sum of the NWPS of individual frames. The exposure consisted of 25 frames with on average  $2.33 \text{ e}^-/\text{pixel}$  per frame recorded using 300 keV electrons, a  $5990 \text{ \AA}$  defocus and a  $1.04 \text{ \AA}$  pixel sampling. The grey scales of the images were set as in Fig. 1.

creases with exposure but  $\sim 100 \text{ e}^-/\text{\AA}^2$  is sufficient to effectively stabilise a film, i.e., the observed Thon ring pattern showed no drift and was stable. As 300 keV electrons can cause displacement damage[14], there was some residual movement but relative to the initial movement this was negligible.

In the first control experiment, the initial 25 frames from a 1.5 second exposure of an area of pre-irradiated carbon were used. The magnification and number of incident electrons per frame were the same as in Fig. 1. The corresponding noise whitened power spectra from the summed image and the sum of the individual power spectra are given in Fig. 2(a) and Fig. 2(b), respectively. In contrast to Fig. 1, the Thon rings are now stronger in the power spectrum of the sum of the frames with the relative strengths being essentially what is expected from 25 images of the same object.

In the second control experiment, a series of 25 images like that in Fig. 2 were taken at adjacent but non-overlapping areas of the pre-irradiated carbon. As there was a slight variation in the height of the carbon film at the different locations the objective lens current was adjusted in order to keep the vari-

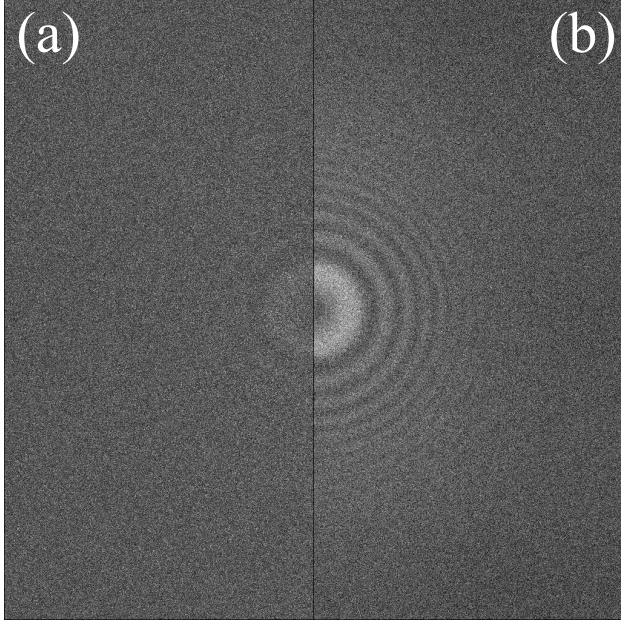


Figure 3: Comparison from a composite exposure of (a) the NWPS obtained from the sum of all the frames and (b) the sum of the NWPS of the individual frames. The composite image consisted of 25 single frames taken from different dose fractionated images of non-overlapping areas in a region of pre-irradiated amorphous carbon. The imaging conditions were the same as in Fig. 2 with the grey scales of the images set as in Fig. 1.

ation in the defocus of the images to within  $\pm 90 \text{ \AA}$ . A composite image of 25 frames was then generated by taking one frame from each of the 25 images. As in Figs. 1 and 2 the corresponding power spectra from the Fourier transform of the sum of the frames from the composite image is given in Fig. 3(a) while that of the sum of the power spectra of the individual frames in the composite image is shown in Fig. 3(b). Like Fig. 1, the Thon rings in Fig. 3 are more visible in the sum of the power spectra than in the power spectrum of the summed image. As expected Fig. 2(b) and Fig. 3(b) are almost identical since they both consist of the sum of 25 power spectra from images of areas with the same thickness of stabilised carbon taken with essentially the same defocus and number of electrons.

In Fig. 2, the carbon atom positions are effectively the same in all the frames while in Fig. 3 there are no correlations between atom positions in the different frames. The similarity of Fig. 1 to Fig. 3 indicates that water molecules in amorphous ice are moving to uncorrelated positions during an exposure.

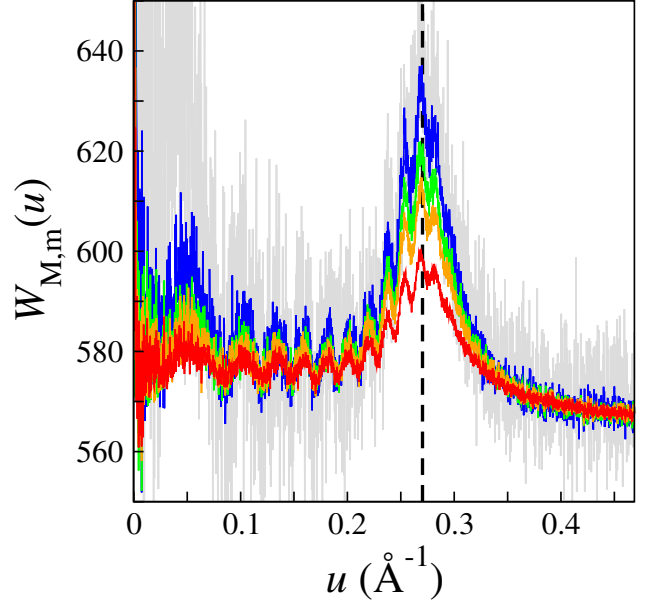


Figure 4: Circularly averaged power spectra,  $W_{120,m}(u)$  as a function of spatial frequency,  $u$ , from 120 frames of image #230804 used in Fig. 1 showing the behaviour with  $m$ . Results for  $m = 1$  (red),  $m = 2$  (orange),  $m = 3$  (green),  $m = 8$  (blue),  $m = 120$  (grey) are shown. Exposure #230804 had  $2.33 \text{ e}^-/\text{pixel}/\text{frame}$  and using Eq. (8) with a DQE of 0.5 for the Falcon II gives an expected average background  $\Gamma = 550$ . The expected noise in the limit of zero spatial frequency from Eq. (8) is  $50\sqrt{m}$  but this decreases with the square root of the spatial frequency as more values are included in the circular average. The vertical dashed line indicates the position of  $1/3.7 \text{ \AA}$  data used in Fig. 5.

Fig. 4 shows the circularly averaged values of  $W_{M,m}(u)$  at selected values of  $m$  obtained from the dose fractionated image series of amorphous ice in exposure #230804 used in Fig. 1. For simplicity in factorisation, only the first 120 of 141 frames were used. The average background value, the magnitude of the associated noise and their variation with  $m$  are in agreement with the predictions of Eq. (8) and Eq. (9). There are some residual correlations within, and between, frames that lead to small systematic variations in  $W_{M,m}(u)$  with  $m$ . These were removed by adding a small  $m$  dependent shift for each  $m > 1$  to ensure that at the Nyquist frequency (in this case  $1/2.08 \text{ \AA}$ )  $W_{M,m}(u) = W_{M,1}(u)$ . The maximum shift required was for  $m = 120$  and corresponded to 5% of the background.

Fig. 5 shows the circularly averaged values of  $W_{M,m}(u)$  as a function of  $m$  at  $u = 1/3.7 \text{ \AA}$  (indicated by the vertical dashed line in Fig. 4) from 120 frames of exposure #23804. Also shown in Fig. 5 are results from a dose fractionated image



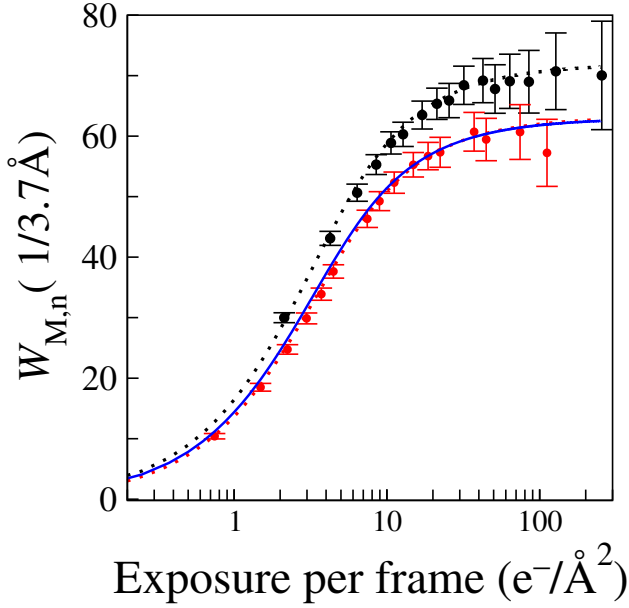


Figure 5: Measured Thon ring modulation from the circularly averaged  $W_{M,m}(u)$  at  $u = 1/3.7\text{\AA}$  as a function of the number of electrons per unit area in the summed frames. The results shown using black bullet (●) are from the first 120 frames of exposure #230804 with  $2.33\text{ e}^{-}/\text{pixel}/\text{frame}$ . The results shown using red bullet (●) are from the first 300 frames of exposure #171528 taken with the same magnification and defocus but over 15 seconds using  $0.85\text{ e}^{-}/\text{pixel}/\text{frame}$  on a different amorphous ice sample. The red and black dotted lines show fits to the corresponding experimental data using Eq. (17). The solid blue curve lies almost on top of the dotted red curve and is simply 0.87 times the dotted black curve. The error bars are based on circularly averaged estimates using Eq. (9).

(#171524) consisting of 300 frames from of a different amorphous ice sample using the same magnification as image #23804 but with an exposure rate of  $0.85\text{ e}^{-}/\text{pixel}/\text{frame}$ . The dotted lines in Fig. 5 are fits to the measured results using Eq. (17) and two adjustable parameters:  $\sigma_0^2$  and a scale factor. The scale factor includes the electron optical terms and is proportional to the total number of electrons in the exposure, the scattering strength and thickness of the amorphous ice sample. Fits to successive dose fractionated images of a fixed area of amorphous ice give essentially the same value for  $\sigma_0^2$  but the scale factor decreases as the sample is thinned by radiolysis. The fitted values of  $\sigma_0^2$  shown in Fig. 5 for images #230804 and #171524 are  $0.38$  and  $0.35\text{ \AA}^2/(\text{e}^{-}/\text{\AA}^2)$ , respectively. There are many sources of systematic error in this analysis and at best these values for  $\sigma_0^2$  should be considered as estimates. Based on these estimates the radiation

damage resulting from one incident  $300\text{ keV e}^{-}/\text{\AA}^2$  is expected to induce a total mean squared motion of  $\sim 1.1\text{ \AA}^2$  in the water molecules of the sample.

For a dose fractionated exposure of  $M$  frames the Thon ring signal given by Eq. (18) (and illustrated in Fig. 5) initially increases linearly with  $m$  but plateaus at higher  $m$ . As the corresponding noise, given by Eq. (9), grows as  $\sqrt{m}$  there is an optimal  $m$ , and hence dose per image, with which to observe Thon rings. Dividing Eq. (18) by  $\sqrt{z}$  and setting the derivative with respect to  $z$  to zero gives a transcendental equation with zero at 2.149. For a given resolution,  $u$ , the optimal number of electrons per unit area,  $d_{\text{opt}}$  in a frame for observing Thon rings is

$$d_{\text{opt}} = 2.149/2\pi^2\sigma_0^2u^2. \quad (19)$$

The peak is not very sharp but for a given dose the Thon rings around  $1/3.7\text{\AA}$  from amorphous ice (assuming  $\sigma_0^2 = 0.37\text{ \AA}^2/(\text{e}^{-}/\text{\AA}^2)$ ) will have the highest signal to noise ratio if each frame has, or successive frames are grouped into blocks with an average exposure of  $\sim 4.0\text{ e}^{-}/\text{\AA}^2$ .

Finally, while Fig. 5 gives the amplitude of the observed Thon ring modulation in  $W_{M,m}(u)$  as  $m$  (and hence the exposure per image) is varied, it is also useful to look at how the corresponding visibility of the Thon ring modulation, i.e., the signal-to-noise ratio, varies. Fig. 6 shows a log-log plot of the variation in the signal-to-noise relative to the corresponding case with  $m = 1$  in the noise whitened power spectra as a function of  $m$ . Results are shown for both the amorphous ice exposures shown in Fig. 5 as well as the pre-irradiation carbon cases shown in Fig. 2 and 3. The results for amorphous ice fall between two extremes, given by a line varying as  $\sqrt{m}$  for the case where the images are of the same object in each frame (such as in Fig. 2 for the images of the same area of pre-irradiated carbon), and in the other extreme of a line varying as  $1/\sqrt{m}$  for the case where the images are of uncorrelated objects in the different frames (such as in Fig. 3 made up of images of different areas of amorphous carbon). The  $\sqrt{m}$  and  $1/\sqrt{m}$  limits indicated by the dotted lines in Fig. 6 simply follow from noting  $W_{M,m}$  as defined in (17), varies as  $m$  in the limit where there is no movement between frames but goes to a constant when there is no correlation between frames while the noise given by Eq. (9) varies as  $\sqrt{m}$ . The signal-to-noise ratio curves for both exposure #23804 and #151524 initially vary as  $\sqrt{m}$  but make the transition to



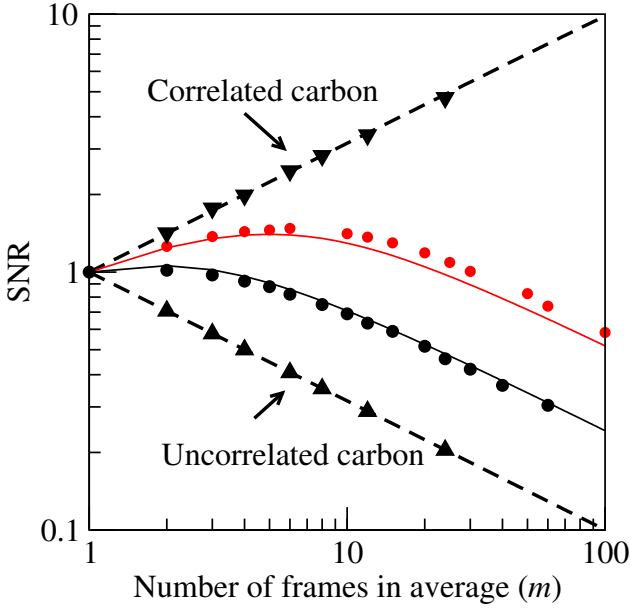


Figure 6: Relative signal-to-noise ratio of Thon rings in the sum of noise whitened power spectra,  $W_{M,m}/W_{M,1}$ , from a dose fractionated exposure of  $M$  frames as a function of the number of successive images in each power spectrum,  $m$ . Results at  $u = 1/9.0 \text{ \AA}$  from 24 frames of the pre-irradiated carbon images used for Fig. 2 ( $\blacktriangledown$ ) and Fig. 3 ( $\blacktriangle$ ) are shown. Results at  $u = 1/3.7 \text{ \AA}$  from 120 frames of image #23804 ( $\bullet$ ) with  $2.33 \text{ e}^-/\text{pixel}$  and 300 frames of image #171524 ( $\bullet$ ) with  $0.85 \text{ e}^-/\text{pixel}$  of Fig. 5 are shown. The results using Eq. (9) for the noise and Eq. (18)) for the signal with  $\sigma_0^2 = 0.37 \text{ \AA}^4/\text{e}^-$  are shown as solid lines.

$1/\sqrt{m}$  for large  $m$ . As expected from Eq. (19) in going from behaving as  $\sqrt{m}$  to  $1/\sqrt{m}$  the amorphous ice curves reach a peak at  $m$  corresponding to  $\sim 4 \text{ e}^-/\text{\AA}^2$ . The solid lines in Fig. 6 show the predicted behaviour of  $g(z)/\sqrt{z}$  in which  $g(z)$  is defined in Eq. (18) with  $z = 2\pi^2\sigma_0^2u^2md$  at  $u = 1/3.7 \text{ \AA}$  with  $\sigma_0^2 = 0.37 \text{ \AA}^2/(\text{e}^-/\text{\AA}^2)$  and  $d = 2.33 \text{ e}^-/\text{frame}$ , (black —), or  $d = 0.85 \text{ e}^-/\text{frame}$  (red —).

## 5. Discussion

The recent introduction of higher performance electron detectors has allowed structures of biological macromolecules to be obtained by single particle cryoEM to higher resolution, with fewer particles and more easily than before [4]. However, these reconstructions still require averaging substantially more particle images than predicted to be necessary by theory [15]. Charging of the specimen and its surroundings as well as physical movement of the specimen during exposure to the first few  $\text{e}^-/\text{\AA}^2$  are

two reasons for this discrepancy.

To observe well defined Thon rings from images of amorphous ice the sample must be neither too thick nor too thin. If the ice film is too thin, the amplitude of the Thon ring signal will simply be too small to be seen amongst the background noise. If the ice film is too thick the Thon signal will also become weaker, especially at high resolution. Part of this reduction comes from the variation in defocus as images of molecules at different heights have Thon ring zeroes at different spatial resolutions, and part is due to increased multiple elastic and inelastic scattering of the electron beam. If an ice film is too thick it is possible to use radiolysis to thin the film to the desired thickness by recording a succession of images. With 300 keV electrons the thickness of an ice film is typically reduced by  $100 \text{ \AA}$  for every  $170 \text{ e}^-/\text{\AA}^2$  of electron dose [16]. From the number of successive images required to completely burn through the ice film used in Fig. 1 we estimate that the image used in Fig. 1 was taken when the ice thickness was between 1000 and 1500  $\text{\AA}$ .

The high number of electrons used in Fig. 1 ( $304 \text{ e}^-/\text{\AA}^2$ ) ensures the Thon rings are clearly visible but is not necessary. With the correct conditions Thon rings can easily be seen with  $26 \text{ e}^-/\text{\AA}^2$ . In fact the Thon ring visibility in the sum of the power spectra from 12 frames of amorphous ice exposure from Fig. 1 is comparable to that seen in the sum of the power spectra of same number of frames from the amorphous carbon results of Fig. 3 (see supplementary Sec. SVIII). The pattern of the Thon rings from amorphous ice differs from that of carbon, with the amorphous ice signal, as in Fig. 1, strongest around  $1/3.7 \text{ \AA}$  while the corresponding pattern from amorphous carbon is strongest at low spatial frequencies. The  $3.7 \text{ \AA}$  resolution signal in amorphous ice comes from planes of next nearest neighbour oxygen atoms of tetrahedrally coordinated water molecules and the strength of this signal indicates that the ice rules of Bernal and Fowler [11] are applicable in amorphous ice.

The major origin of beam induced motion in an amorphous ice film is from radiolysis rather than knock-on damage [17]. The rate of mass loss from a thin film is observed to be almost independent of film thickness and so most of the radiolysis fragments remain within the film [17]. This so called cage-effect, allows many of the radiolysis fragments in ice to recombine but some such as  $\text{O}_2$  and  $\text{H}_2\text{O}_2$ , will accumulate and re-orient the surrounding water molecules. The successful fits shown in Fig. 5

do however support the simple Gaussian Markov Process description of Sec.2.5. In practice irradiation of a plunge frozen amorphous ice film will also result in collective motion of local regions due to stress relief within the film and charging from the emission of secondary electrons.

From our experimental observation we deduce that water molecules, each with a molecular mass of 18 Da, move an RMS distance of  $\sim 1\text{\AA}$  for each  $e^-/\text{\AA}^2$ . A typical cryoEM exposure having  $25 e^-/\text{\AA}^2$  will therefore result in a RMS displacement of water molecules by  $\sim 5\text{\AA}$ . In the same way as the thermal motion of water molecules results in Brownian motion, the beam-induced motion of water molecules will also be expected to displace embedded protein molecules. In a  $25 e^-/\text{\AA}^2$  exposure a protein molecule of 100 kDa, such as hexokinase, embedded in this film of randomly diffusing molecules would be expected to have an RMS displacement of  $\sim 1.0\text{\AA}$  (hexokinase with a MW of 100 kDa has a 20-40x smaller diffusion coefficient than water, and so should move  $\sim 4$ -6x less, according to the Stokes-Einstein equation for diffusion [18] in which the diffusion coefficient varies as  $1/\text{MW}^{1/3}$ ). For a protein molecule of 25 kDa, the beam-induced random motion would be higher at  $\sim 1.5\text{\AA}$ , and for a ribosome of 2.5 MDa somewhat lower at  $\sim 0.7\text{\AA}$ . This additional B-factor, which for hexokinase would correspond to  $\sim 25\text{\AA}^2$ , produces some extra image blurring on top of that resulting from other effects such as intrinsic radiation damage to the macromolecular assembly. We can thus conclude that random, Brownian type of beam-induced motion of biological structures is unlikely to be one of the limiting factors in attaining high-resolution structures using single particle cryoEM approaches. Only for very small particles at resolutions of  $2\text{\AA}$  or beyond is this type of beam-induced motion likely to be a fundamental limitation.

It can be argued that the observed degree of beam-induced motion of water molecules in amorphous ice during an exposure is actually of positive benefit in cryoEM. If water molecules moved much less during irradiation they would contribute a strong background, just as there is from carbon films, that would decrease the accuracy of the orientation determination in single particle cryoEM. If water molecules moved more then so too would the embedded macromolecules and the images of these would be more blurred.

## Acknowledgments and declaration of interest

The authors acknowledge funding from the Medical Research Council, grant number U105184322. We would also like to thank Garib Murshudov and Nigel Unwin for their helpful comments.

## References

- [1] F. Thon, Zur defokussierungsabhaengigkeit des phasenkontrastes bei der elektronenmikroskopischen abbildung, *Z. Naturforsch* 21 (a) (1966) 476–478.
- [2] J. Dubochet, J. Lepault, R. Freeman, J. A. Berriman, J.-C. Homo, Electron microscopy of frozen water and aqueous solutions, *Journal of Microscopy* 128 (3) (1982) 219–237.
- [3] J. Dubochet, M. Adrian, J. J. Chang, J. C. Homo, J. Lepault, A. W. McDowell, P. Shultz, Cryo-electron microscopy of vitrified specimens, *Quarterly Reviews of Biophysics* 21 (1988) 129–228.
- [4] W. Kühlbrandt, The resolution revolution, *Science* 343 (6178) (2014) 1443–1444. doi:10.1126/science.1251652.
- [5] L. Reimer, K. Helmut, *Transmission Electron Microscopy - Physics of Image Formation*, 5th Edition, Springer, 2008.
- [6] J. C. H. Spence, *High-Resolution Electron Microscopy*, 4th Edition, Oxford University Press, 2013.
- [7] G. McMullan, A. Faruqi, D. Clare, R. Henderson, Comparison of optimal performance at 300keV of three direct electron detectors for use in low dose electron microscopy, *Ultramicroscopy* 147 (0) (2014) 156–163. doi:10.1016/j.ultramicro.2014.08.002.
- [8] S. O. Rice, Mathematical analysis of random noise, *Bell System Technical Journal* 23 (3) (1944) 282–332. doi:10.1002/j.1538-7305.1944.tb00874.x.
- [9] H. J. Zweig, Detective quantum efficiency of photodetectors with some amplification mechanisms, *Journal of the Optical Society of America* 55 (5) (1965) 525–528. doi:10.1364/JOSA.55.000525.
- [10] H. G. Heide, Observations on ice layers, *Ultramicroscopy* 14 (3) (1984) 271–278. doi:http://dx.doi.org/10.1016/0304-3991(84)90095-0.
- [11] J. D. Bernal, R. H. Fowler, A theory of water and ionic solution, with particular reference to hydrogen and hydroxyl ions, *The Journal of Chemical Physics* 1 (8) (1933) 515–548. doi:10.1063/1.1749327.
- [12] J. R. Bellare, H. T. Davis, L. E. Scriven, Y. Talmon, Controlled environment vitrification system: An improved sample preparation technique, *Journal of Electron Microscopy Technique* 10 (1) (1988) 87–111. doi:10.1002/jemt.1060100111.
- [13] J. A. Mindell, N. Grigorieff, Accurate determination of local defocus and specimen tilt in electron microscopy, *Journal of Structural Biology* 142 (3) (2003) 334–347. doi:http://dx.doi.org/10.1016/S1047-8477(03)00069-8.
- [14] R. Egerton, P. Li, M. Malac, Radiation damage in the TEM and SEM, *Micron* 35 (6) (2004) 399–409. doi:10.1016/j.micron.2004.02.003.
- [15] R. Henderson, The potential and limitations of neutrons, electrons and X-rays for atomic resolution microscopy of unstained biological molecules, *Quarterly Reviews of Biophysics* 28 (02) (1995) 171–193.

- [16] E. R. Wright, C. V. Iancu, W. F. Tivol, G. J. Jensen, Observations on the behavior of vitreous ice at 82 and 12 K, *Journal of Structural Biology* 153 (3) (2006) 241–252. doi:<http://dx.doi.org/10.1016/j.jsb.2005.12.003>.
- [17] H.-G. Heide, E. Zeitler, The physical behavior of solid water at low temperatures and the embedding of electron microscopical specimens, *Ultramicroscopy* 16 (2) (1985) 151–160. doi:[http://dx.doi.org/10.1016/0304-3991\(85\)90070-1](http://dx.doi.org/10.1016/0304-3991(85)90070-1).
- [18] A. Einstein, Über die von der molekularkinetischen theorie der wärme geforderte bewegung von in ruhenden flüssigkeiten suspendierten teilchen, *Annalen der Physik* 322 (1905) 549–560.

# Supplementary material: Thon rings from amorphous ice and implications of beam-induced Brownian motion in single particle electron cryo-microscopy

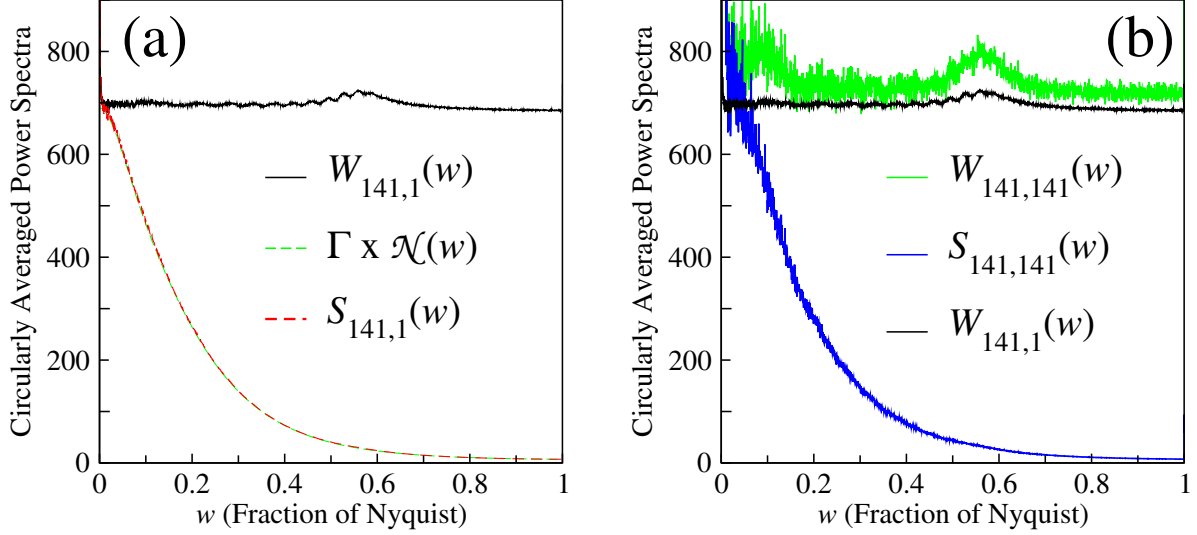


Figure SI: Comparison of the spatial frequency dependence of the circularly averaged sum of power spectra and noise whitened power spectra from the 141 frame dose fractionated exposure (image #230804) of amorphous ice used for Fig. 1. The spatial frequency,  $w$  is measured as a fraction of the Nyquist frequency ( $1/2.08\text{\AA}$ ). In (a), the sum of the power spectra of the individual images ( $S_{141,1}(w)$  and  $W_{141,1}(w)$ ) along with  $\Gamma \times \mathcal{N}(w)$  using  $\Gamma = 684$  are given. In (b), the circularly averaged power spectrum of the sum of the 141 frames ( $S_{141,141}(w)$  and  $W_{141,141}(w)$ ) along with  $W_{141,1}(w)$  are shown.

## SVI. Comparison of $S(u)$ and $W(u)$ from exposure #230804 of Fig.1

The effect of noise whitening is illustrated in Fig. SI(a) which compares the spatial frequency dependence of the sum of the circularly averaged power spectrum,  $S_{141,1}$  and noise whitened power spectrum,  $W_{141,1}$ , (using the notation of Eq. (8)) obtained from the 141 frames used to generate Fig. 1 of the text. The variation with spatial frequency of  $S_{141,1}(w)$  is essentially that of  $\mathcal{N}(w)$ . The multiplicative factor,  $\Gamma$ , relating  $S_{141,1}(w)$  and  $\mathcal{N}(w)$  is given in Eq. (7). The measured value for  $\Gamma$  of 684 is within 5% of that from Eq. (11) with a DQE(0) of  $\sim 0.5$  and dose of  $2.33 \text{ e}^-/\text{pixel}$ . The noise whitening produced by division of  $S(w)$  by  $\mathcal{N}(w)$  removes this variation, producing a flat background above which the amorphous ice Thon ring signal around  $1/3.7\text{\AA}$ , now enhanced by  $1/\mathcal{N}(w) \sim 24$ , can clearly be seen. Noise whitening can be applied to both the sum of the power spectra as shown in SI(a) and the power spectrum of the sum of the frames given in SI(b). The lower noise in the sum of the power spectra provides a more stringent test for the noise whitening procedure; the success of this is clearly illustrated by the featureless flat background in Figs. 1 – 3 of the main text.

Residual correlations in the detector, in particular from the applied linear pixel gain correction, lead to a difference in the value for the sum of the power spectra versus the power spectrum of the image sum. This is illustrated in Fig. SI(b) where the value of  $W_{141,141}(w)$  is 5% greater than that of  $W_{141,1}$ .

Fig. SII(a) compares the spatial frequency dependence of the circularly averaged noise whitened sum of power spectra and that of noise whitened power spectrum of the sum of the frames. For convenience, an offset equal to Nyquist frequency value has been subtracted. The Thon ring signal is bigger in the power spectrum of the sum of the frames but the background noise is also bigger (by a factor of  $\sqrt{141} \sim 12$ ). In Fig. 1 of the main text, the Thon ring signal from the amorphous ice appears stronger in the sum of the

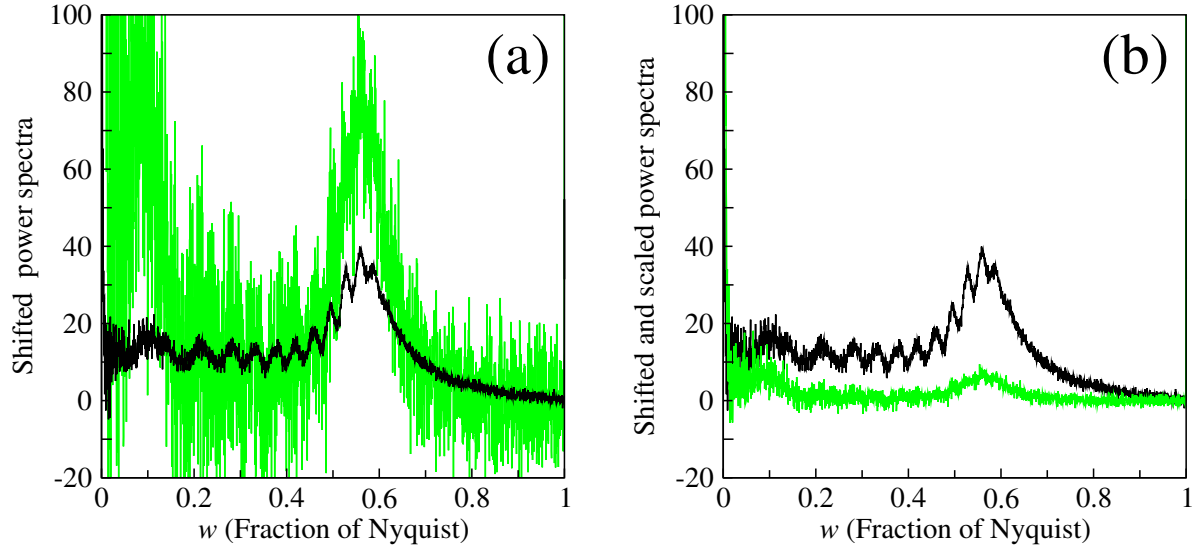


Figure SII: Comparison of the circularly averaged Thon ring signal from the dose fractionated exposure (image #230804) of amorphous ice as seen in the sum of the noise whitened power spectra (black) with that in the power spectrum of the sum of the image frames (green). The background offset, seen in Fig. SI(b), has been removed by subtracting the average value near the Nyquist frequency. The results from Fig. SI(b) shifted in this way are shown in (a) while in (b) the visibility of the Thon ring signal is shown by rescaling the power spectrum of the sum of the images in (a) so that it has the same noise level as sum of the power spectra curve.

power spectra (Fig. 1(b)) rather than in the power spectrum of the sum of the images (Fig. 1(a)). This is because the images in Fig. 1 have been scaled so that background noise has the same amplitude. This effect of this is illustrated in Fig. SII(b) and is obtained by dividing the circularly averaged power spectrum of the sum frames by  $\sqrt{141}$  so that the noise level in the two plots (green and black) is the same.

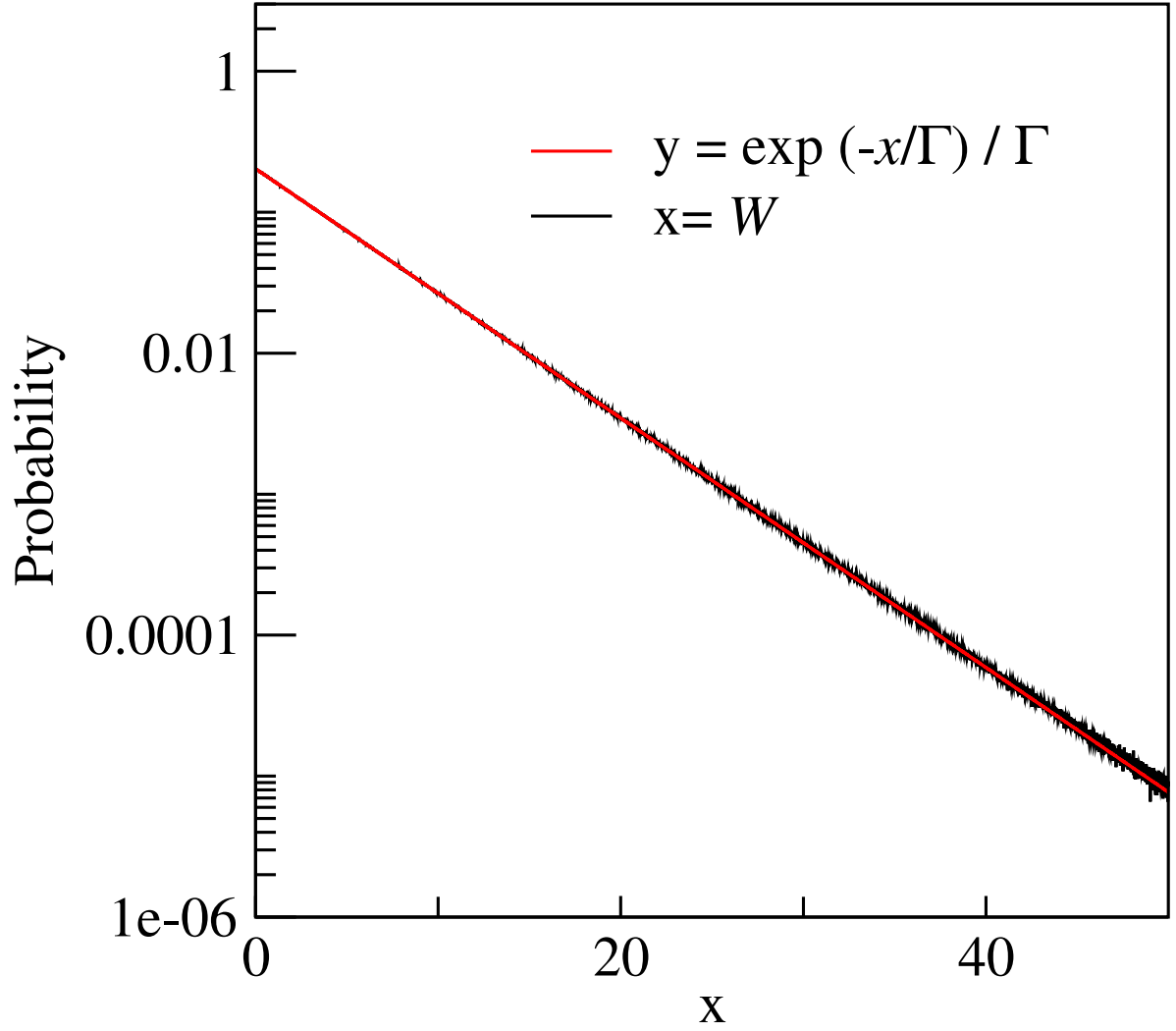


Figure SIII: Histogram of the 141 frames noise whitened power spectra from image #230804 of amorphous ice used in Fig. 1. The exponential distribution fit, —, to the measured histogram, —, is with  $\Gamma = 4.91$ .

### SVII. Statistics of noise whitened power spectra

As discussed in the text, the distribution of the of values in a noise whitened power spectra of the Falcon II is completely described by its mean value  $\Gamma \sim n/\text{DQE}(0)$  in which  $n$  is the mean number of incident electrons per frame, through exponential distribution of Eq. (8). To illustrate this, the histogram of values in noise whitened power spectra of the 141 frames used in Fig. 1 is given in Fig. SIII. The measured histogram is an excellent fit to an exponential distribution with parameter  $\Gamma = 4.91$  (which differs by 5% from the estimate based on  $\text{DQE}(0) = 0.5$  and  $n = 2.33 \text{ e}^-/\text{pixel}/\text{frame}$ ).

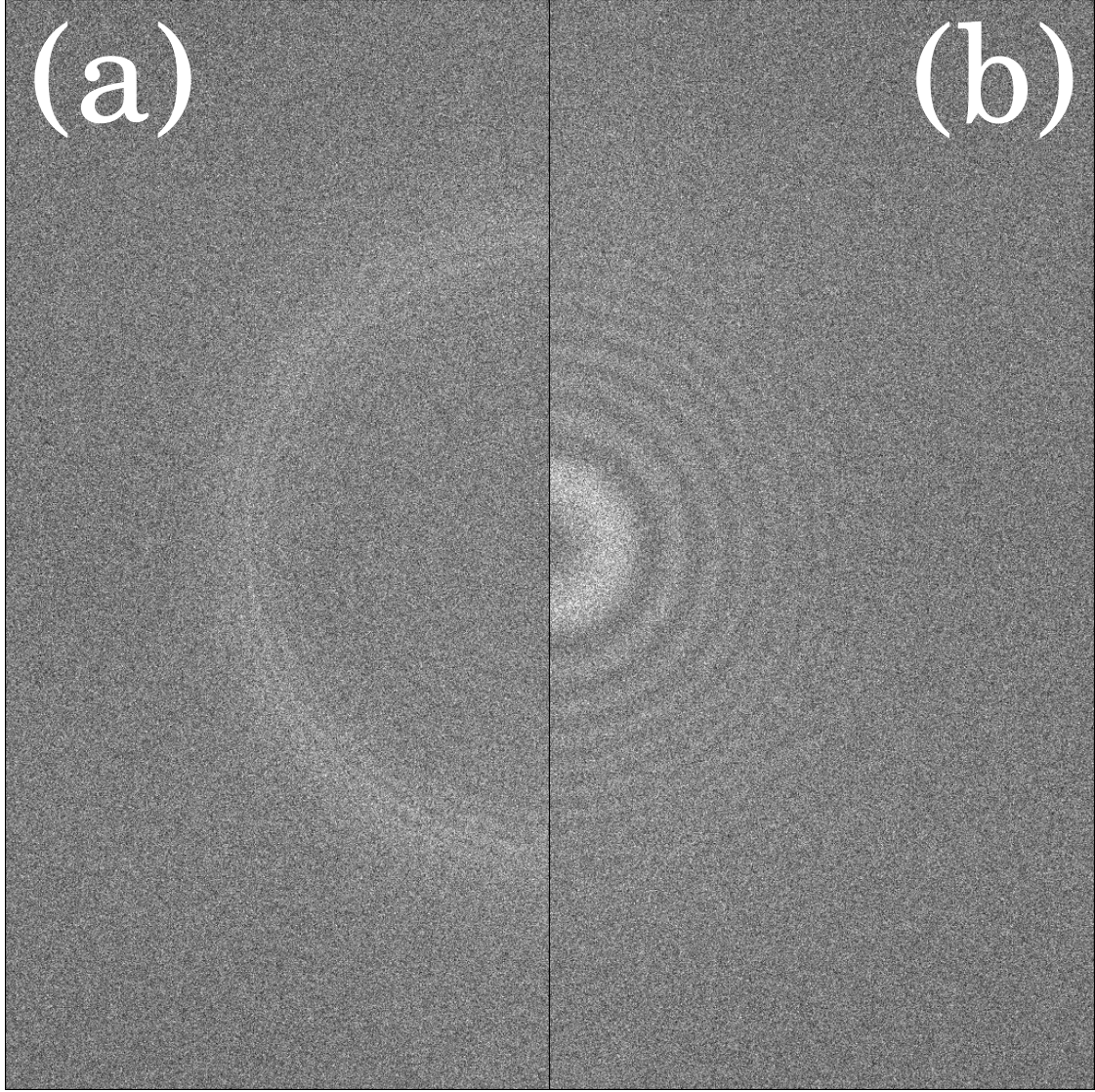


Figure SIV: (a) Sum of noise whitened power spectra from the first 12 frames of image #230804 from Fig. 1. (b) Sum of noise whitened power spectra from the first 12 frames of the pre-irradiated carbon image used in Fig. 2. The same magnification and total dose ( $25.9 \sim 12 \times 2.33/1.04^2 \text{ e}^-/\text{\AA}^2$ ) were used in both (a) and (b). The Thon rings from amorphous ice around  $1/3.7 \text{ \AA}$  are stronger than those from the pre-irradiated carbon sample.

#### **SVIII. Comparison at $26 \text{ e}^-/\text{\AA}^2$ of Thon rings from amorphous ice with those from pre-irradiated amorphous carbon**

Fig. SIV(a) shows the Thon rings obtained from the sum of the first 12 noise-whitened power spectra, corresponding to  $25.9 \text{ e}^-/\text{\AA}^2$  from the 141 used in Fig. 1. For comparison Fig. SIV(b) shows the corresponding sum of noise whitened power spectra from images of pre-irradiated carbon in Fig. 2. While the Thon rings from carbon are stronger at low spatial frequency, around  $1/3.7 \text{ \AA}$  those from the amorphous ice sample are stronger. This is more clearly illustrated in the circular averages shown in Fig. SV.

Fig. SV(a) shows the circular averages of the sum of the noise whitened power spectra shown in Fig. SIV. In Fig. SV(b) the noise whitened power spectrum of the sum of the 12 pre-irradiated carbon frames used



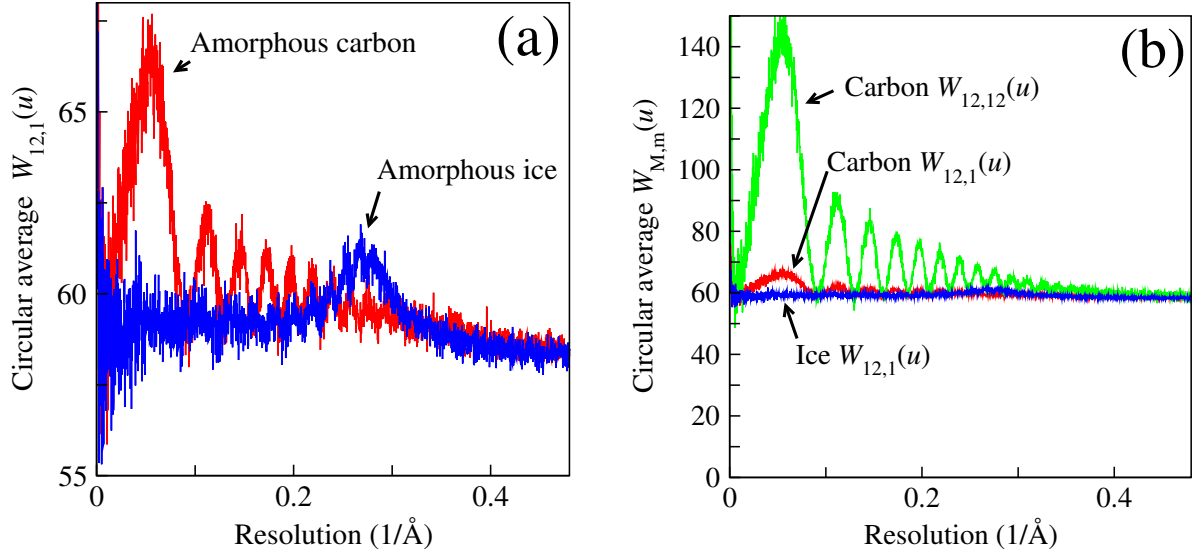


Figure SV: Comparison of the circular averages of the noise whitened power spectra obtained with  $\sim 26e^-/\text{\AA}^2$  from amorphous ice and pre-irradiated carbon. The  $W_{12,1}(u)$  circular averages of the amorphous ice (blue) and pre-irradiated carbon (red) sums of noise whitened power spectra shown in (a). In (b) the corresponding circular average of the power spectrum,  $W_{12,12}(u)$ , from the sum of the 12 frames of pre-irradiated amorphous carbon is shown.

in Fig. SV is compared with the sum of 12 power spectra given in Fig. SV(a). As the pre-irradiated carbon does not move during an exposure the Thon ring signal adds coherently with increasing number of frames. The Thon ring modulation in the sum of the images,  $W_{12,12}(u)$ , is 12 times that in the corresponding sum of power spectra,  $W_{12,1}(u)$ . At the Nyquist frequency the image consists almost entirely of noise and the power spectra of the sum of the images is equal to the sum of the power spectra. The noise in the power spectrum of the sum is however  $\sqrt{12}$  times that in the sum of the power spectra.

## SIX. Calculation of normalised noise power spectrum, $\mathcal{N}(u)$

The energy lost by incident high energy electrons passing through the lightly doped semi-conducting sensitive layer of a CMOS sensor such as the Falcon II, produces electron/hole pair excitations. The sensitive layer is surrounded by heavily P-doped layers into which the holes are free to escape but the negatively charged electron excitations are trapped due to the potential resulting from the differential doping. An incident high energy electron is recorded via the voltage drop on reverse biased diodes formed by a heavily N-doped implants on the surface of the sensitive layer resulting for collection of the electron excitations. The number of electron-hole pairs generated by an incident high energy electron, and hence the signal, depends on the length of the incident electrons trajectory through the sensitive layer. The thick sensitive layer of the Falcon II results in a large average signal but the thickness of the sensitive layer allows electrons to diffuse relatively large distances before they are finally collected. This diffusion results in a poor modulation transfer function, MTF, even with the relatively large ( $14\ \mu\text{m}$ ) pixel size of the Falcon II. The diffusion acts as a low-pass filter and while it lowers the MTF it has only a small effect on the detective quantum efficiency, DQE. In other words the spatial distribution of the signal deposited in the detector by an incident electron, described by the point spread function (PSF), is mainly determined by electron/hole diffusion and not scattering of the primary incident electron (at least for incident 300 keV electrons). The Fourier transform of the point spread function determines the intrinsic spatial frequency response of the detector and its square describes the noise power spectrum. In a real pixellated detector the noise power spectrum also includes pixel modulation terms of the form  $\sin(x)/x$  from integration over the pixel and contributions aliased back from spatial frequencies beyond the Nyquist frequency of the pixellated sampling.

As shown in [7] the  $\mathcal{N}(u)$  for the Falcon II detector is to a good approximation given by

$$\mathcal{N}(u, v) = \sum_{\mathbf{G}} \left( \sin(\pi a u_G) \sin(\pi a v_G) \text{MTF}_0(\sqrt{u_G^2 + v_G^2}) \right)^2 \quad (\text{SXX})$$

where  $a$  is the pixel pitch, the sum is over the low order reciprocal lattice vectors needed to describe the aliasing,  $u_G$  and  $v_G$  are the spatial frequency components i.e.,  $u_G = u + G_u$ , and  $\text{MTF}_0$  is the Fourier transform of the intrinsic PSF. In [7]  $\mathcal{N}(u, v)$  was calculated from the  $\text{MTF}_0$  obtained from the experimentally measured MTF. While this works well (reducing the variation in the power spectra to a few percent), the higher signal to noise in the longer exposures used in the present work show small systematic variations. The results presented in Figs. 1-3 were therefore obtained using a fit to a radial function  $\phi(u)$ , effectively  $\text{MTF}_0(u)^2$ , from zero to twice the Nyquist frequency of the measured noise power spectra using the functional form in Eq. (SXX).

The simplest way to calculate  $\mathcal{N}(u, v)$  is to average the noise power spectra of many frames and apply the symmetry from the square pixel array. This leaves some residual noise and the problem of finding the overall normalisation. In the present work a radial function,  $\phi(u)$ , was used to fit the symmetrized sum of the noise power spectra via

$$S(u, v) \sim \sum_{\mathbf{G}} \sin^2(\pi a u_G) \sin^2(\pi a v_G) \phi(\sqrt{u_G^2 + v_G^2}). \quad (\text{SXXI})$$

The overall normalisation was found by using a single Gaussian function in  $\phi(u)$  to fit the low spatial frequency limit and a smooth general fit to the remainder via a b-spline fit that was penalty weighted to ensure smoothness and non-negative values. A more detailed description of this and its implementation will be presented elsewhere.